Supplementary Information for

New Insights into Aliovalent Substituted Halide Solid Electrolytes for Cobalt-Free All-Solid-State Batteries

Changhong Wang,[a,b,c,‡] Shuo Wang[d, ‡] Xudong Liu,[a] Yanlong Wu,[e] Ruizhi Yu,[a] Hui, Duan,[a] Jung Tae Kim,[a] Huan Huang,[e] Jiantao Wang,[c,e,] Yifei Mo,[d,*] Xueliang Sun[a,b,*]*

Affiliations

[a] *Department of Mechanical and Materials Engineering, University of Western Ontario, 1151 Richmond St, London, Ontario, N6A 3K7, Canada.*

[b] Eastern Institute for Advanced Study, Eastern Institute of Technology, Ningbo, Zhejiang 3150200, P.R. China

[c] *Glabat Solid-State Battery Inc., 700 Collip Circle, London, ON, N6G 4X8, Canada*

[d] *Department of Materials Science and Engineering, University of Maryland, College Park, MD, 20742 USA*

[e] *China Automotive Battery Research Institute Co. Ltd., Beijing P.C.101407, China.*

[‡] These authors contributed equally to this work.

[*]Email: wangjt@glabat.com, yfmo@umd.edu, and xsun9@uwo.ca

Experimental methods

Synthesis of Li-Lu-Zr-Cl solid solutions. Lithium chloride (LiCl, Alfa Aesar, 99.9%), Lutetium chloride (LuCl$_3$, Alfa Aesar, 99.99%), zirconium chloride (ZrCl$_4$, Alfa Aesar, 99.9%) were used as starting precursors. The stoichiometric amounts of starting precursors were thoroughly mixed and pressed into a pellet. Then the pellets were sealed in a quartz tube under vacuum (around 10 Pa), heated at 650 °C for 12 hours, and cooled down naturally. The agglomerated product was ground into a mortar to get the final powder for characterization.

Materials Characterization. The X-ray diffraction (XRD) patterns were obtained over the range of 10º to 120º (2θ) using Cu Kα X-ray radiation with λ = 1.54178 Å (Bruker AXS D8 Advance). The ground materials were loaded and sealed in an air-tight holder to avoid air exposure to protect them from ambient air. The data for the XRD Rietveld refinement were collected by scanning 5s per step with one step of 0.02 ° and refined by GSAS.[1] Scanning electron microscopy (SEM) images were recorded using a Hitachi S-4800 field emission SEM equipped with energy dispersive spectroscopy (EDS).

Electrochemical Characterizations. The ionic conductivities of the synthesized Li-Lu-Zr-Cl solid solutions were measured by AC impedance spectroscopy. Powder samples were cold pressed into pellets at 640 MPa in a 10 mm diameter stainless steel die for 10 minutes. Two indium foils were attached to improve the interfacial contact for EIS measurements. Impedance spectroscopy was performed on a VMP3 potentiostat/galvanostat (Biologic) frequency range from 7 MHz to 1 Hz. The obtained impedance spectroscopy was performed on the EC-Lab software. The electronic conductivity of the Li$_{2.5}$Lu$_{0.5}$Zr$_{0.5}$Cl$_6$ was measured according to the direct current (DC) polarization curve using ion-blocking electrodes of stainless steel. The externally applied voltages range from 0.1-0.5 V. All cell preparation processes were conducted inside an Ar-filled glove box. The electrochemical stability was evaluated by cyclic voltammetry (CV) measurements using versatile multichannel potentiostat 3/Z (VMP3) with a Li/ Li$_6$PS$_5$Cl/ Li$_{2.5}$Lu$_{0.5}$Zr$_{0.5}$Cl$_6$ / Li$_{2.5}$Lu$_{0.5}$Zr$_{0.5}$Cl$_6$+carbon cell in a scan range of 0 to 5 V (vs. Li$^+$/Li) at 0.1 mV s^{-1}. The mass loading of Li$_{2.5}$Lu$_{0.5}$Zr$_{0.5}$Cl$_6$+carbon is 7mg.

To prepare cathode composites, commercial LiMn$_2$O$_4$ and as-prepared Li$_{2.5}$Lu$_{0.5}$Zr$_{0.5}$Cl$_6$ with a mass ratio of 70:30 were thoroughly ground together in an agate mortar for 10 min. 50 mg of the as-synthesized Li$_{2.5}$Lu$_{0.5}$Zr$_{0.5}$Cl$_6$ and 30 mg of Li$_6$PS$_5$Cl were compressed at 1 ton to form a solid-state electrolyte layer. 10 mg cathode composites were then spread on one side of Li$_{2.5}$Lu$_{0.5}$Zr$_{0.5}$Cl$_6$ pellets and pressed at 3.5 tons. Then a piece of the lithium-indium alloy was put on another side of Li$_6$PS$_5$Cl and pressed at 1 ton. The cells were cycled in the voltage range of 3.0-4.3 V (vs. Li$^+$/Li) by homemade model cells using a

Neware cycler (Shenzhen, China) at room temperature. The testing pressure for all-solid-state batteries is 50 MPa. For long-term cycling stability, the testing pressure was set to 150 MPa. For liquid cells, the mass loading of $LiMn_2O_4$ is 6.88~7.45 mg.cm^{-2}.

A solvent-free dry-film process was used to fabricate single-layer $Li_{2.5}Lu_{0.5}Zr_{0.5}Cl_6$-based all-solid-state pouch cells. Using polytetrafluoroethylene (PTFE) as a binder, 100μm cathode composite film with a mass loading is 12.9 mg.cm^{-2} (active material loading=8.9 mg.cm^{-2}), 100 μm $Li_{2.5}Lu_{0.5}Zr_{0.5}Cl_6$ film, and 100 μm Li_6PS_5Cl film were fabricated and stacked together by a cold iso-static press. Then a 50μm In-Li film was attached and pressed at 50 MPa. Finally, the 3×3cm^2 all-solid-state pouch cell was sealed with plastic aluminum foil and tested under 10MPa at 0.05C.

First-principles calculation. All density functional theory (DFT) calculations are performed with Vienna Ab initio Simulation Package (VASP) within the projector augmented wave (PAW) approach.[2, 3] Generalized gradient approximation (GGA) with the Perdew–Burke–Ernzerhof (PBE) functional was used.[4] The plane-wave energy cutoff, k-points density, and other convergence parameters in all DFT static calculations were consistent with the Materials Project (MP).[5] The Li-ion and its vacant-site contents are obtained based on their crystal structure and stoichiometric ratio in their chemical formula.

Structural ordering. In experimental refined structures, the Zr and Lu co-occupy the octahedral 4c sites. Li has partial occupancy on octahedral 8d sites in solid solutions of $Li_{3-x}Lu_{1-x}Zr_xCl_6$ (0<x<1). Given the disordering of Li, Lu, and Zr in crystal structures, we first determined the configurations using the same scheme in our previous studies[6, 7] for $Li_{2.25}Lu_{0.25}Zr_{0.75}Cl_6$, $Li_{2.5}Lu_{0.5}Zr_{0.5}Cl_6$, and $Li_{2.75}Lu_{0.75}Zr_{0.25}Cl_6$, respectively. For each composition, we first generated 5000 structures by randomizing the disordered sites with probabilities as the corresponding partial occupancies in a 1×1×2 supercell. Among all these structures, 50 symmetrically distinct structures with minimal electrostatic energies were selected for DFT calculations, and the lowest-energy structure was identified as the ground state for further calculations.

Ab initio molecular dynamics simulations. We performed *ab initio* molecular dynamics (AIMD) simulations using 1×1×2 supercell models, which contain eight formula units of $Li_{2.25}Lu_{0.25}Zr_{0.75}Cl_6$, $Li_{2.5}Lu_{0.5}Zr_{0.5}Cl_6$, and $Li_{2.75}Lu_{0.75}Zr_{0.25}Cl_6$, respectively. NVT ensemble with Nosé-Hoover thermostat, non-spin mode, a time step of 2 fs, and Γ-centered 1×1×1 k-point grid was used. The structures were heated from 100 K to targeted temperatures (400-900 K) for 2 ps first, and then the simulations lasted 50-400 ps until the diffusivity converged in a relative standard deviation between 25% to 35%. The uncertainty came from the stochastic process of ionic hopping and was evaluated according to the number

of hopping events in our previous report.[8] The diffusivity coefficient D was calculated by the mean square displacement (MSD) over time:

$$D = \frac{\text{MSD}(\Delta t)}{2d\Delta t} = \frac{1}{2Nd\Delta t}\sum_{i=1}^{N}\left\langle [r_i(t + \Delta t) - r_i(t)]^2 \right\rangle_t$$

Where d is the diffusion dimension, N is the total number of diffusion ions, $r_i(t)$ is the position of the i-th ion at time t, and the bracket represents averaging over t. Arrhenius relation is used to get activation energy and to extrapolate ionic conductivity at the desired temperature:

$$D = D_0 exp\left(\frac{-E_a}{k_B T}\right)$$

Where E_a is the activation energy, D_0 is the pre-exponential factor, T is the temperature, and k_B is the Boltzmann constant.

Electrochemical window. We used the grand potential phase diagram to identify the phase equilibria $C_{eq}(C, \mu_{Li})$ of a given phase with the composition C in equilibrium with the Li reservoir at chemical potential μ_{Li} referenced to Li metal. As in previous studies,[9, 10] the stable electrochemical window of the phase was estimated as the range of μ_{Li}, where the phase is neither oxidized nor reduced.
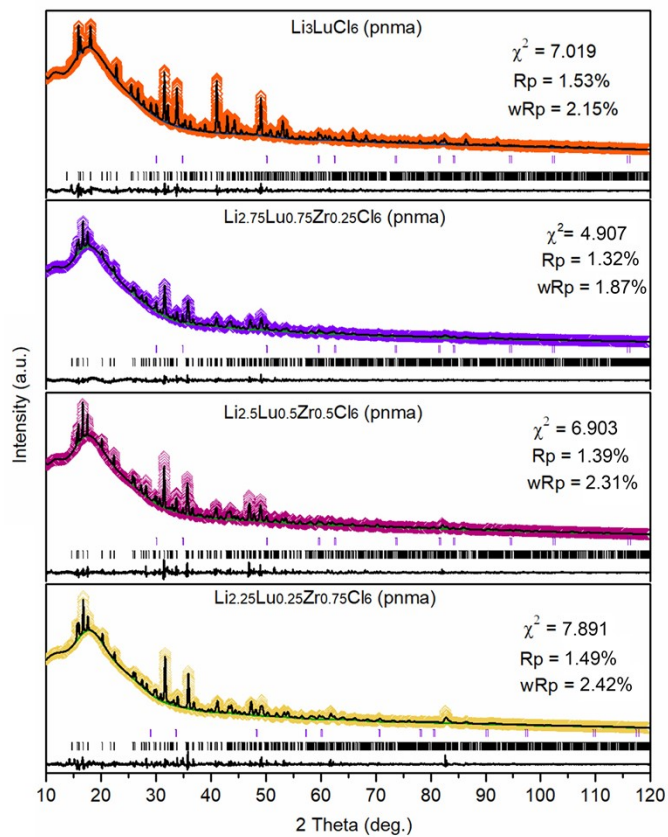
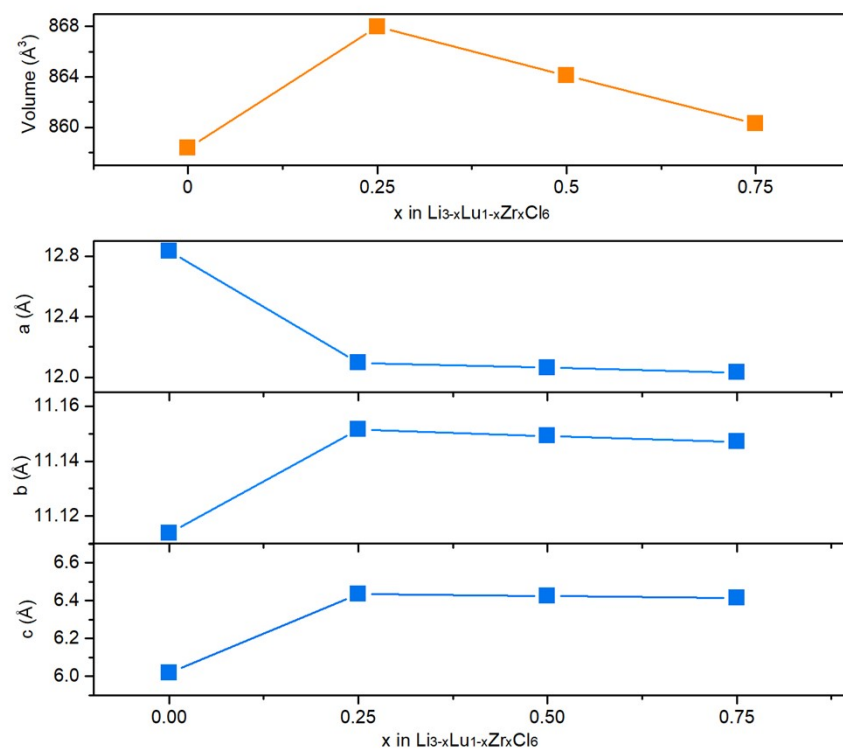**Figure S1**. **Structural analysis of Li-Lu-Zr-Cl solid solutions.** Rietveld refinement of Li_3LuCl_6 and Zr-doped Li_3LuCl_6 solid solutions.

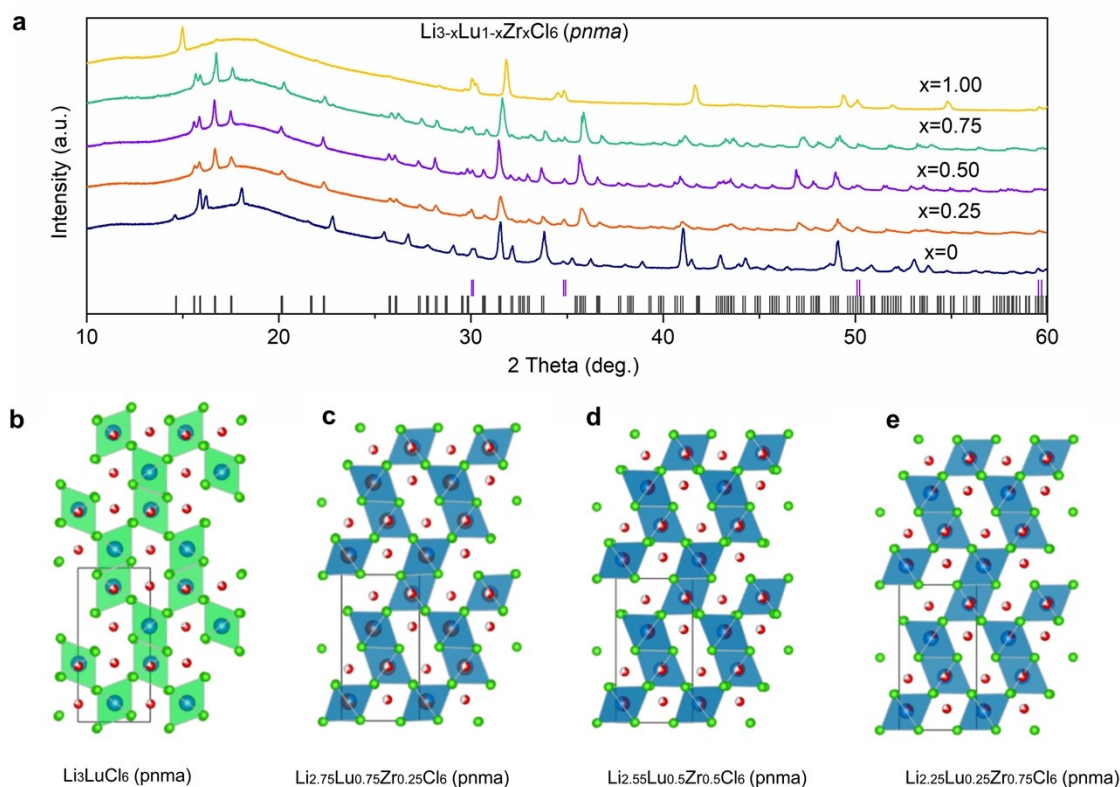**Figure S2**. The unit cell volume lattice parameters of $Li_{3-x}Lu_{1-x}Zr_xCl_6$ ($0 \leq x \leq 1$) solid solutions.

Figure S3. (a) XRD results of Li-Lu-Zr-Cl solid solutions and corresponding crystal structure. (b) Li_3LuCl_6. (c) $Li_{2.75}Lu_{0.75}Zr_{0.25}Cl_6$. (d) $Li_{2.5}Lu_{0.5}Zr_{0.5}Cl_6$. (e) $Li_{2.725}Lu_{0.25}Zr_{0.75}Cl_6$. No obvious structural change is identified when the Zr content increases from 0.25 to 0.75.
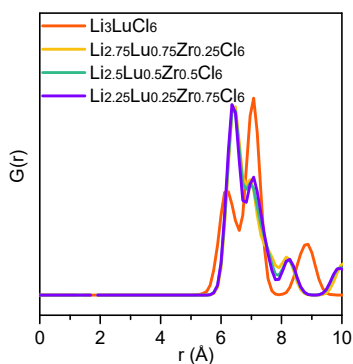

Figure S4. The radial distribution function g(r) of Lu/Zr cation sublattice in Pnma-I (green) and Pnma-II (red) phase from AIMD simulations at 400K.
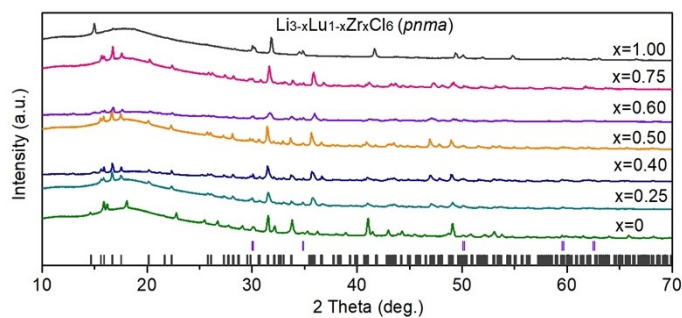
Figure S5. XRD patterns of $Li_{3-x}Lu_{1-x}Zr_xCl_6$ ($0 \leq x \leq 1$) solid solutions (x=0, 0.25, 0.4, 0.5, 0.6, 0.75, and 1).
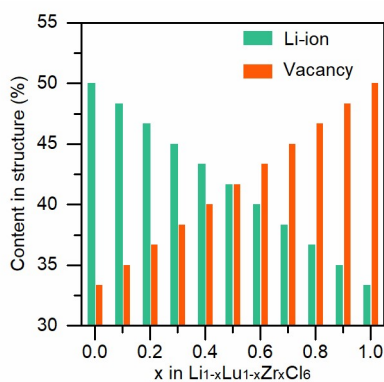

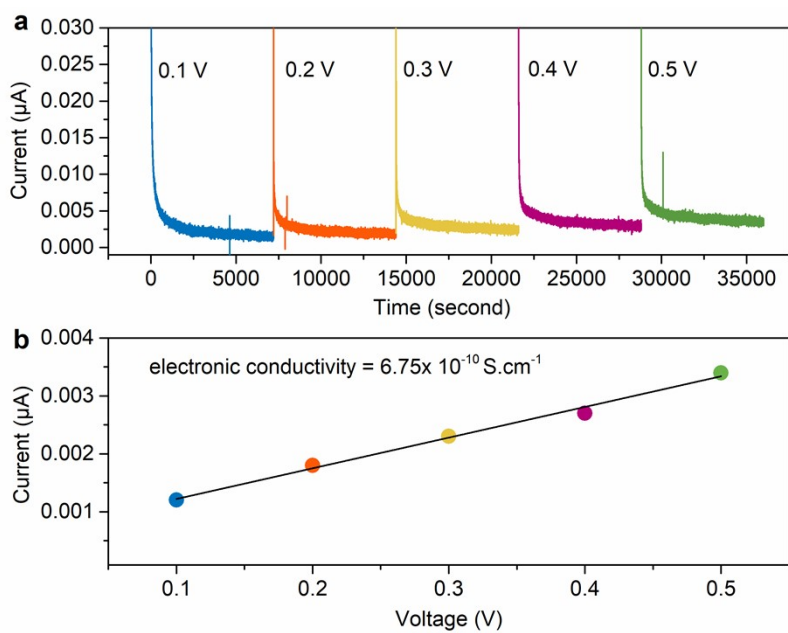**Figure S6.** The Li-ion and vacant-site concentration in Li-Lu-Zr-Cl solid solutions.

Figure S7. Electronic conductivity measurement of $Li_{2.5}Lu_{0.5}Zr_{0.5}Cl_6$. (a) DC polarization curves under different biases. (b) Electronic conductivity.

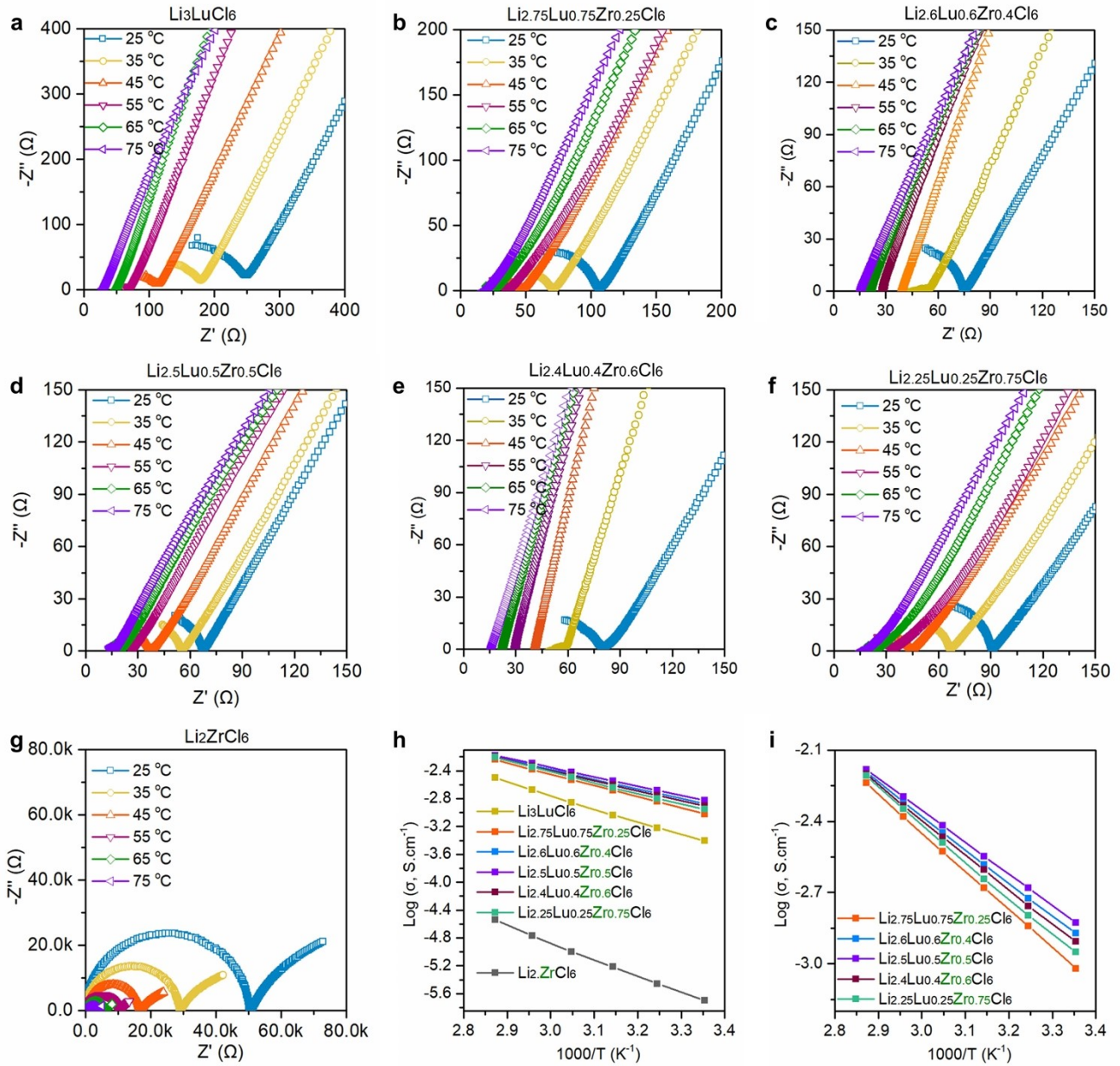**Figure S8. Temperature-dependent EIS profiles of solid electrolytes.** (a) Li_3LuCl_6. (b) $Li_{2.75}Lu_{0.75}Zr_{0.25}Cl_6$. (c) $Li_{2.6}Lu_{0.6}Zr_{0.4}Cl_6$. (d) $Li_{2.5}Lu_{0.5}Zr_{0.5}Cl_6$. (e) $Li_{2.4}Lu_{0.4}Zr_{0.6}Cl_6$. (f) $Li_{2.25}Lu_{0.25}Zr_{0.75}Cl_6$. (g) Li_2ZrCl_6. (h) and (i) Arrhenius plots of Li-Lu-Zr-Cl solid solutions.
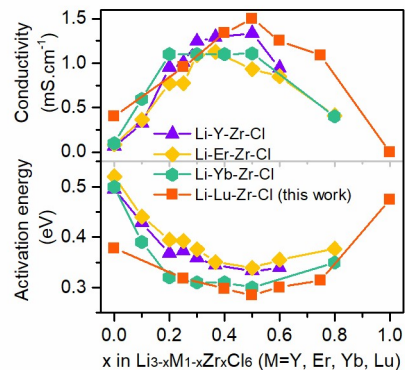
Figure S9. The literature data were reproduced with permission from references Li-Y-Zr-Cl,[11] Li-Er-Zr-Cl,[11]Li-Yb-Zr-Cl.[12]

Figure S10. Arrhenius plot of Li diffusion in Li-Lu-Zr-Cl solid solutions from AIMD simulation.
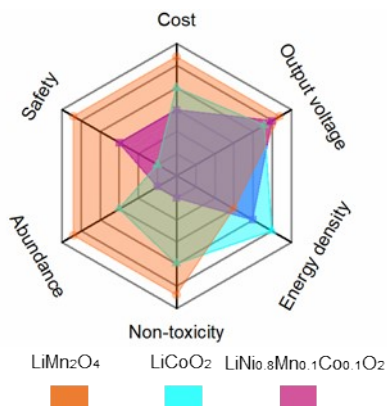
Figure S11. Radar plot to show the advantages of $LiMn_2O_4$ in comparison to common layered cathodes.
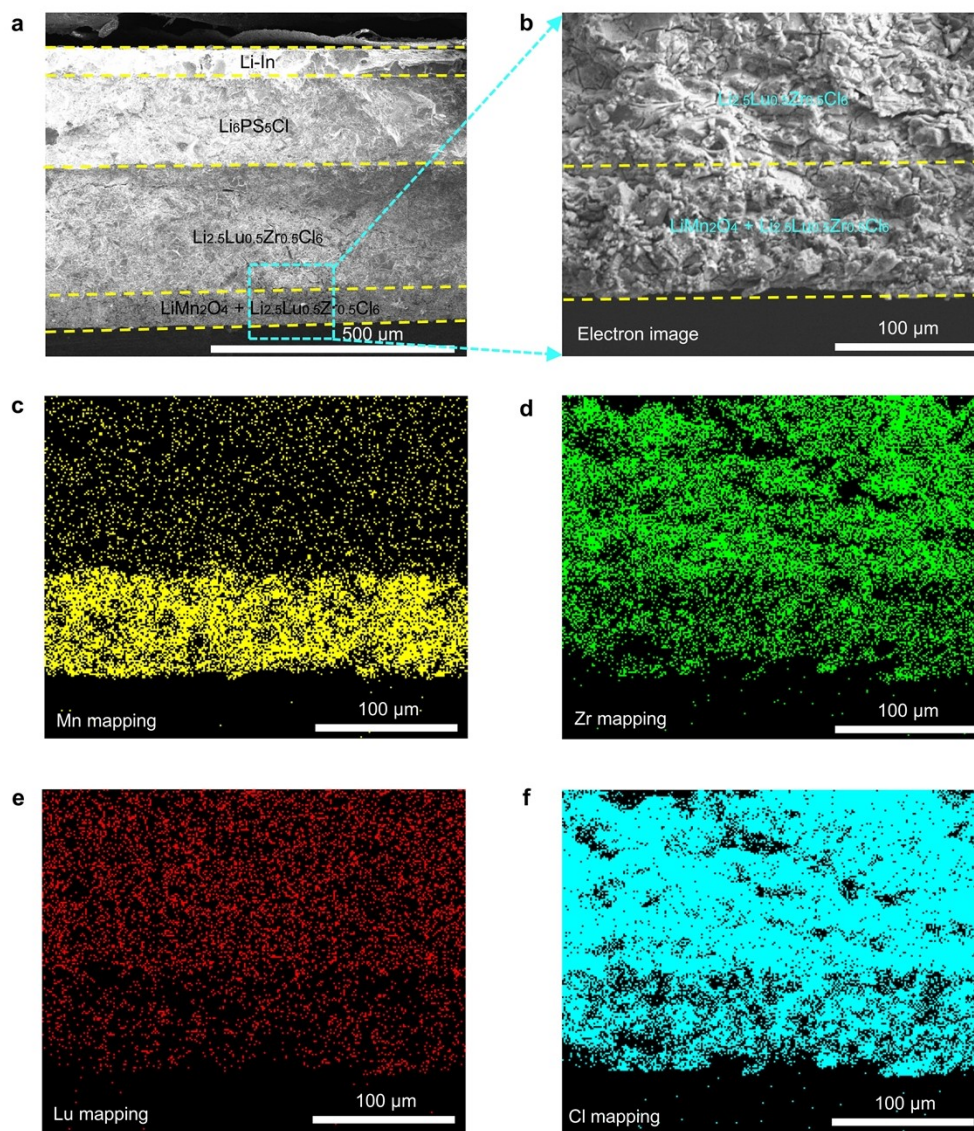
Figure S12. Cross-sectional SEM image of $Li_{2.5}Lu_{0.5}Zr_{0.5}Cl_6$-based all-solid-state batteries using $LiMn_2O_4$ as the cathode.

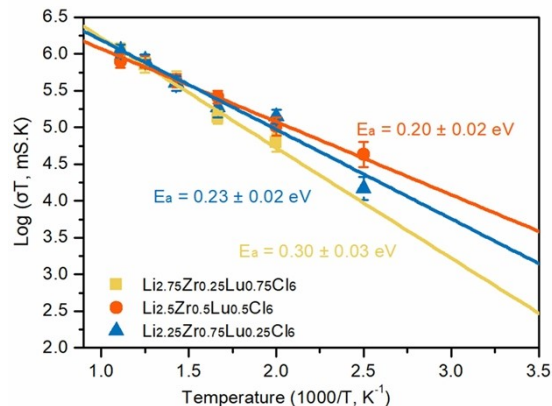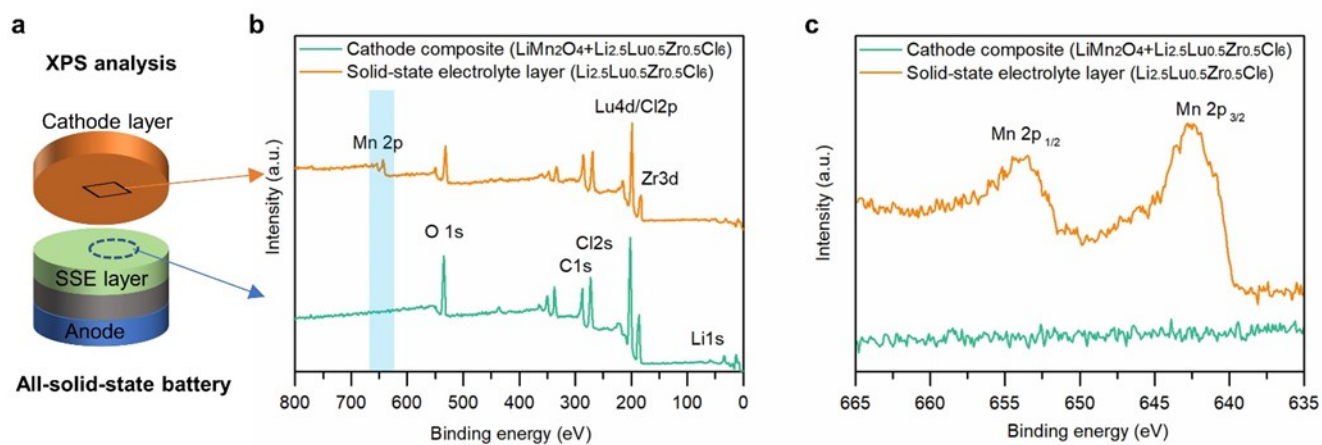**Figure S13**. XPS analyses of cathode composites and Li-Lu-Zr-Cl solid-state electrolyte after cycling. (a) Schematic illustration of XPS analysis sample positions. (b) Full survey. (c) high-resolution Mn 2p spectra.

Figure S14. The discharge curves of halide-based LiMn$_2$O$_4$-based all-solid-state batteries under different C-rates.

Figure S15. The cycling stability of LiMn$_2$O$_4$-based all-solid-state batteries.

Figure S16. EIS profile of cobalt-free LiMn$_2$O$_4$-based all-solid-state batteries.

Table S1. Crystal characteristics of common ternary halide electrolytes.

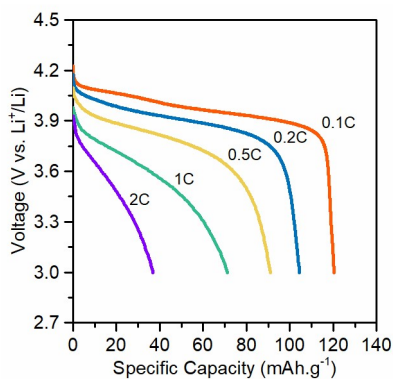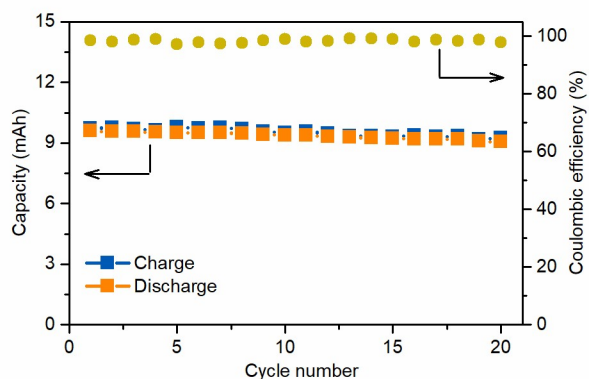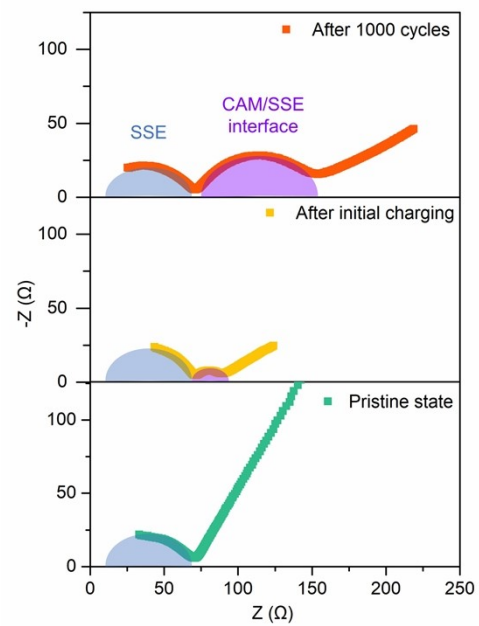|	Space group	Crystal system	Ionic conductivity@25 ºC	Activation energy (eV)	Electrochemical window (V vs Li$^+$/Li)
Li$_3$YCl$_6$-lc	P-3m1		0.51	0.4	0.62 ~ 4.2
Li$_3$TbCl$_6$	P-3m1		0.22	0.39	0.6 ~ 4.21
Li$_3$DyCl$_6$	P-3m1	Trigonal (hcp)	0.12	0.42	0.62 ~ 4.21
Li$_3$HoCl$_6$	P-3m1		0.29	0.45	0.64 ~ 4.25
Li$_3$ErCl$_6$-lc	P-3m1		0.33	0.41	0.63 ~ 4.26
Li$_3$TmCl$_6$	P-3m1		0.11	0.41	0.62~ 4.22
Li$_3$YbCl$_6$	p-3m1, Pnma		0.064 0.32	unknown	
Li$_3$LuCl$_6$	Pnma	Orthorhombic (hcp)	0.4	0.375	0.6~4.2
Li$_{3-x}$M$_{1-x}$Zr$_x$Cl$_6$	Pnma		0.4~1.5	2.7~3.8	1.75~4.25
Li$_3$ScCl$_6$	C2/m	Monoclinic	3	0.362	0.87 ~ 4.21
Li$_3$InCl$_6$	C2/m	(ccp)	2.02	0.347	2.38 ~ 4.3

Table S2. Atomic coordinates, occupation factor and isotropic displacement parameters of Li$_3$LuCl$_6$ obtained from Rietveld refinement (space group *pnma*), a =12.83390(8) Å, b = 11.11386(12) Å, c = 6.01780(8) Å, α = β = γ=90.0000°. Volume= 858.344(15). It should be noted that the Li position has some variations due to its weak interaction with X-ray.

Atom	x	y	z	Occ.	Site	Sym.	Uiso
Li(1)	0.10808(17)	0.07437(19)	0.03443 (15)	0.750	8d	1	0.01601(11)
Li(2)	0.1083(8)	0.08779(18)	0.52644(16)	0.750	8d	1	0.02895(19)
Cl(3)	0.20700(19)	0.57727(26)	0.2719(11)	1.000	8d	1	0.0317(5)
Cl(4)	0.45536(20)	0.11651(21)	0.2505(11)	1.000	8d	1	0.0317(5)
Cl(5)	0.03728 (26)	1/4	0.7274(11)	1.000	4c	m	0.0286(5)
Cl(6)	0.20523(26)	1/4	0.2417(13)	1.000	4c	m	0.0286(5)
Lu(7)	0.37705(13)	1/4	0.0109(4)	1.000	4c	m	0.03060(32)

Table S3. Atomic coordinates, occupation factor and isotropic displacement parameters of Li$_{2.75}$Lu$_{0.75}$Zr$_{0.25}$Cl$_6$ obtained from Rietveld refinement (space group *pnma*), a =12.09488(15) Å, b = 11.15151(10) Å, c = 6.4352(33) Å, α = β = γ=90.0000°. Volume= 867.959(21).

Atom	x	y	z	Occ.	Site	Sym.	Uiso
Li(1)	0.1285(8)	0.08989(19)	0.10165(15)	0.625	8d	1	0.03906(21)
Li(2)	0.35534(18)	0.09963(18)	0.09411(16)	0.625	8d	1	0.02895(19)
Cl(3)	0.00329(21)	0.57422(19)	0.24990(15)	1.000	8d	1	0.03833(10)

Cl(4)	0.25315(21)	0.0869(18)	0.40387(16)	1.000	8d	1	0.05084(12)
Cl(5)	0.00033(22)	1/4	0.24220(6)	1.000	4c	m	0.06155 (11)
Cl(6)	0.74658(24)	1/4	0.55717(22)	1.000	4c	m	0.03833(11)
Lu(7)	0.36855(14)	1/4	0.59589(25)	0.750	4c	m	0.03375(5)
Zr(8)	0.368555(14)	1/4	0.595889(25)	0.250	4c	m	0.03375(5)

Table S4. Atomic coordinates, occupation factor and isotropic displacement parameters of $Li_{2.5}Lu_{0.5}Zr_{0.5}Cl_6$ obtained from Rietveld refinement (space group *pnma*), a =12.06326(24) Å, b = 11.14916(17) Å, c = 6.42478(22) Å, $\alpha = \beta = \gamma$=90.0000°. Volume= 864.102(17).

Atom	x	y	z	Occ.	Site	Sym.	Uiso
Li(1)	0.13471(17)	0.0779(9)	0.09319(14)	0.6875	8d	1	0.02868(26)
Li(2)	0.3534(8)	0.08437(22)	0.11436(16)	0.6875	8d	1	0.01857(22)
Cl(3)	0.00122(29)	0.57498(35)	0.25291(22)	1.000	8d	1	0.036226(14)
Cl(4)	0.25302(09)	0.0821(4)	0.43221(14)	1.000	8d	1	0.048776(11)
Cl(5)	0.00088(12)	1/4	0.24711(13)	1.000	4c	m	0.04817(10)
Cl(6)	0.74774(24)	1/4	0.55009(14)	1.000	4c	m	0.03275(11)
Lu(7)	0.36896(22)	1/4	0.59091(22)	0.500	4c	m	0.02022(9)
Zr(8)	0.36896(22)	1/4	0.59091(22)	0.500	4c	m	0.02022(9)

Table S5. Atomic coordinates, occupation factor and isotropic displacement parameters of $Li_{2.25}Lu_{0.25}Zr_{0.75}Cl_6$ obtained from Rietveld refinement (space group *pnma*), a =12.03107(30) Å, b = 11.14705(19) Å, c = 6.41483(22) Å, $\alpha = \beta = \gamma$=90.0000°. Volume= 860.298(87)

Atom	x	y	z	Occ.	Site	Sym.	Uiso
Li(1)	0.1272(23)	0.0760(24)	0.097(7)	0.5625	8d	1	0.01361(22)
Li(2)	0.3496(19)	0.0747(24)	0.079(6)	0.5625	8d	1	0.00350(25)
Cl(3)	0.00559(26)	0.58289(32)	0.2446(4)	1.000	8d	1	0.02426(12)
Cl(4)	0.25576(17)	0.08735(31)	0.4184(7)	1.000	8d	1	0.03702 (10)
Cl(5)	0.0049(8)	1/4	0.2352(7)	1.000	4c	m	0.04142(13)
Cl(6)	0.7516(4)	1/4	0.5755(9)	1.000	4c	m	0.02544(10)
Lu(7)	0.36881(11)	1/4	0.59170(25)	0.250	4c	m	0.03322(6)
Zr(8)	0.36881(11)	1/4	0.5917025)	0.750	4c	m	0.03322(6)

References

1.   B. H. Toby and R. B. Von Dreele, *J. Appl. Crystallogr.*, 2013, **46**, 544-549.
2.   G. Kresse and J. Furthmüller, *Phys. Rev. B*, 1996, **54**, 11169-11186.
3.   P. E. Blöchl, *Phys. Rev. B*, 1994, **50**, 17953-17979.
4.   J. P. Perdew, M. Ernzerhof and K. Burke, *J. Chem. Phys.*, 1996, **105**, 9982-9985.
5.   A. Jain, G. Hautier, C. J. Moore, S. Ping Ong, C. C. Fischer, T. Mueller, K. A. Persson and G. Ceder, *Comput. Mater. Sci.*, 2011, **50**, 2295-2310.
6.   X. He and Y. Mo, *Phys. Chem. Chem. Phys.*, 2015, **17**, 18035-18044.
7.   J. Liang, X. Li, S. Wang, K. R. Adair, W. Li, Y. Zhao, C. Wang, Y. Hu, L. Zhang and S. Zhao, *J. Am. Chem. Soc.*, 2020, **142**, 7012-7022.
8.   X. He, Y. Zhu, A. Epstein and Y. Mo, *Npj Comput. Mater.*, 2018, **4**, 18.
9.   Y. Zhu, X. He and Y. Mo, *ACS Appl. Mater. Interfaces*, 2015, **7**, 23685-23693.
10.   Y. Zhu, X. He and Y. Mo, *J. Mater. Chem. A*, 2016, **4**, 3253-3266.
11.   K.-H. Park, K. Kaup, A. Assoud, Q. Zhang, X. Wu and L. F. Nazar, *ACS Energy Lett.*, 2020, **5**, 533-539.
12.   S. Y. Kim, K. Kaup, K.-H. Park, A. Assoud, L. Zhou, J. Liu, X. Wu and L. F. Nazar, *ACS Mater. Lett.*, 2021, **3**, 930-938.